Research Square

Preprints are preliminary reports that have not undergone peer review.
They should not be considered conclusive, used to inform clinical practice,
or referenced by the media as validated information.

Practical wavelength selection for Quantum-Augmented Networks (QuANets) over shared optical fiber

Nitin Jha

njha1@students.kennesaw.edu

Kennesaw State University

Prateek Paudel

Kennesaw State University

Abhishek Parakh

Kennesaw State University

Article

Keywords:

Posted Date: November 20th, 2026

DOI: https://doi.org/10.21203/rs.3.rs-11569853/v1

License: This work is licensed under a Creative Commons Attribution 4.0 International License.
Read Full License

Additional Declarations: No competing interests reported.

Practical wavelength selection for Quantum-Augmented Networks (QuANets) over shared optical fiber

Nitin Jha[1,*], **Prateek Paudel**[1,+], **and Abhishek Parakh**[1,+]

[1]Kennesaw State University, GA, USA
[*]Corresponding author: njha1@students.kennesaw.edu
[+]These authors contributed equally to this work

ABSTRACT

Sharing optical fiber with classical traffic requires quantum wavelength selection to balance logical fidelity, block acceptance and classical reception. Here we develop a wavelength-selection framework for an error-corrected three-stage quantum communication protocol. Assuming independent thermal backgrounds, ideal one-photon acceptance and ideal recovery, we derive an accepted qubit channel and a key-independent lower bound on conditional logical entanglement fidelity. Combining this bound with block acceptance defines a yield bound for wavelength selection over evaluated candidates. For the Steane code at 5 km per traversal and -10 dBm per classical channel, the largest fidelity certificate occurs near 1537 nm, whereas the largest yield bound occurs near 1551 nm. Along the 1.25 Gb/s classical link-budget curve with 0.2% base error, the yield bound crosses 10^{-6} between 10 and 11 km, while fidelity remains certified at 0.99 or higher through 30 km. Yield therefore restricts certified coexistence before fidelity under these conditions.

1 Introduction

Quantum communication is moving from isolated point-to-point experiments towards integration with existing optical communication infrastructure. Several recent studies have examined the engineering requirements involved in operating quantum links as part of larger communication networks. These include deployment over installed metropolitan fiber, integration with networking equipment, synchronization and stabilization of quantum links, dynamic switching and routing, and the simultaneous operation of quantum and classical network services[1–3]. Large testbeds have also demonstrated heterogeneous quantum networks integrated with the commercial optical infrastructure. For example, the Madrid Quantum Communication Infrastructure (MadQCI) demonstrated a software-defined quantum key distribution (QKD) network using equipment from multiple vendors across different production sites with shared classical communication infrastructure[4]. Other field trials have also demonstrated dynamically switched networks supporting entanglement distribution and high-capacity classical traffic within the same metropolitan infrastructure[5]. More recent work has explored entanglement distribution with coexisting classical signals used for synchronization and compensation of fiber fluctuations[6]. Quantum-augmented networks (QuANets) integrate quantum resources with classical infrastructure to support selected communication and security functions[7–10]. For shared-fiber deployments, wavelength selection must meet the quantum protocol's fidelity and yield requirements at classical launch powers sufficient to close the data link.

Dedicated fiber isolates quantum signals from classical traffic in the same fiber, but does not eliminate attenuation or other imperfections of the quantum link. Providing separate fiber can also increase deployment cost and constrain the use of existing infrastructure. An alternative is wavelength-division multiplexing (WDM), in which quantum and classical channels share an optical fiber at different carrier wavelengths. Such coexistence has been demonstrated experimentally across a range of configurations, including discrete-variable quantum key distribution (DV-QKD) with high-bit-rate classical traffic[11,12], continuous-variable QKD (CV-QKD) with dense coherent WDM channels[13], and most recently, high-capacity quantum-classical transmission over spatially multiplexed fiber infrastructures[14]. The large difference in optical power between classical and quantum channels, however, makes coexistence fundamentally asymmetric. Classical channels carry much higher optical powers than quantum signals, so interference that is negligible at a classical receiver can be significant at a quantum receiver. Spontaneous Raman Scattering (SpRS) is widely identified as one of the dominant features in a quantum-classical fiber coexistence. This matters because the Raman spectrum extends over a broad wavelength range and can thus introduce photons directly into the quantum receiver band. Imperfect filter isolation also allows classical power to leak into quantum channels. Fiber nonlinearities generate additional spectral components through four-wave mixing (FWM). Cross-phase modulation

(XPM) can convert classical intensity fluctuations into phase fluctuations. For the polarization encoding considered here, its effect on the qubit depends on the differential phase between the two polarization components. A phase common to both components does not change the qubit state. Limiting these impairments requires suitable wavelength placement, launch powers, propagation directions and filter isolation, together with a model of the fiber's nonlinear response.

Several studies have examined the coexistence of classical and quantum signals over shared optical fiber. Experimental studies have shown that temporal filtering, spectral filtering, reduced classical launch power, and appropriate spectral separation can substantially improve QKD coexistence performance[11–13]. Other studies have addressed spectral resource allocation, such as different wavelength assignment methods to reduce Raman and FWM contamination[15]. Recent work has incorporated coexistence effects into dynamic routing and spectrum allocation in hybrid quantum-classical dense wavelength-division multiplexing (DWDM) networks[16]. Together, these studies show that wavelength placement is an important design consideration in mitigating coexistence-induced impairments. They also suggest that suitable wavelength-selection strategies depend on the underlying communication protocol, fiber characteristics, channel configuration, and operating conditions.

Several wavelength-allocation studies have evaluated QKD coexistence using measures such as quantum bit error rate (QBER), signal-to-noise ratio, and secret-key rate [15,17,18]. For encoded quantum communication involving repeated channel traversals, wavelength selection must additionally account for the receiver acceptance rule and the correction capability of the quantum code over the complete exchange. Consequently, the wavelength that minimizes an individual optical-noise contribution need not maximize the accepted contribution to logical-state fidelity. This question is relevant to the three-stage protocol, in which the quantum signal traverses the channel three times [19,20]. Multi-photon implementations have been demonstrated[21], and the protocol's behavior under collective-rotation noise has been analyzed [22]. An extension incorporates Calderbank–Shor–Steane (CSS) quantum error correction into the three-stage construction[20]. Here, we study a single-photon polarization encoding of the physical qubits and an ideal receiver that accepts the one-photon subspace after the final traversal. Under this receiver model, acceptance and preservation of the input quantum state are distinct: background photons can contribute to accepted outcomes. We therefore evaluate block acceptance, conditional logical entanglement fidelity, and their product separately.

In this work, we develop an optical-to-logical framework for wavelength selection in a CSS-encoded three-stage protocol[20] sharing fiber with a fixed classical WDM deployment. Under a specified thermal-background model and independent local imperfections, we derive an accepted optical qubit channel and a lower bound on the conditional logical entanglement fidelity after ideal recovery. We combine this bound with the block acceptance probability to define a lower-bound entanglement-fidelity yield. This objective identifies a selected quantum wavelength, wavelengths satisfying prescribed fidelity and yield certificates, and wavelengths attaining near-optimal values of the lower-bound objective. The remaining work is structured as follows. Section 2 defines the optical channel, logical fidelity bounds, and wavelength-selection problem. Section 3 presents numerical verification, wavelength optimization, and sensitivity analyses. Section 4 discusses the assumptions and implications for shared optical infrastructure.

2 Methods

We evaluate the CSS-encoded three-stage protocol [20] in a shared quantum–classical fiber configuration. Wavelength-dependent optical impairments are mapped to an accepted physical-qubit channel through an explicit receiver model. The resulting channel determines a lower bound on logical entanglement fidelity after ideal recovery. We select the quantum wavelength that maximizes the lower bound on entanglement-fidelity yield while satisfying a prescribed conditional-fidelity certificate.

2.1 System Architecture

We consider two users, Alice and Bob, connected by a standard single-mode optical fiber of length L. The three-stage protocol sends the quantum signal from Alice to Bob, back to Alice, and then to Bob again. In the basic configuration, classical traffic propagates from Alice to Bob throughout the exchange. The classical channels therefore co-propagate with the quantum signal during traversals 1 and 3 and counter-propagate during traversal 2. The classical deployment consists of N_c channels with fixed center wavelengths $\Lambda_c = \{\lambda_{c_1}, \ldots, \lambda_{c_{N_c}}\}$.

Their launch powers P_{c_i} are specified at the fiber input. We select the quantum wavelength while keeping the classical wavelengths fixed. Higher classical launch powers increase the background noise at the quantum receiver. For the link-budget comparisons, we adopt the operating-power curve,

$$P_{c,\min}(L) = S_{\mathrm{rx}} + \alpha_c L + IL_{\mathrm{demux}} + M_{\mathrm{sys}}, \tag{1}$$

in dBm, where S_{rx} is the classical receiver sensitivity, α_c is the largest attenuation among the classical channels in $\mathrm{dB\,km^{-1}}$, and L is the fiber length in km. We assume $IL_{\mathrm{demux}} = 3$ dB and $M_{\mathrm{sys}} = 3$ dB. Classical powers are specified at the fiber input. An upstream transmitter must additionally compensate for the input multiplexer loss to deliver the stated fiber-input power.

Let $\Omega_{\mathrm{hw}} \subseteq [\lambda_{\min}, \lambda_{\max}]$ denote the wavelength range supported by the modeled source, receiver, and optical components. The corresponding optical frequencies are

$$f_{c_i} = \frac{c}{\lambda_{c_i}}, \qquad f_q = \frac{c}{\lambda_q}, \tag{2}$$

where c is the speed of light in vacuum. We use frequency to evaluate channel spacing and nonlinear mixing, and report the selected quantum wavelengths in wavelength units. The numerical simulation uses 35 active classical carriers on a 100 GHz grid spanning 191.6–195.9 THz. The unoccupied positions are 192.0, 192.1, 192.2, 192.3, 192.4, 192.5, 192.6, 193.2 and 195.0 THz. Classical traffic propagates from Alice to Bob throughout the exchange.

For a minimum carrier separation Δf_g and an additional frequency clearance $\delta_g \geq 0$, define

$$\Omega_q(\delta_g) = \left\{ \lambda_q \in \Omega_{\mathrm{hw}} : |c/\lambda_q - f_{c_i}| \geq \Delta f_g + \delta_g, \quad \forall i \right\}. \tag{3}$$

Unless stated otherwise, Ω_q denotes $\Omega_q(\delta_g)$ at the nominal clearance $\delta_g = 1$ GHz, chosen below. The clearance δ_g constrains carrier separation. Fidelity is evaluated at the selected frequency. We perform the numerical optimization over a finite set of candidate frequencies $\mathscr{F}_{\mathrm{eval}}$. The evaluated wavelength domain is

$$\Omega_q^{\mathrm{eval}}(\delta_g) = \left\{ \lambda_q \in \Omega_q(\delta_g) : c/\lambda_q \in \mathscr{F}_{\mathrm{eval}} \right\}. \tag{4}$$

The candidate set $\mathscr{F}_{\mathrm{eval}}$ includes a uniform grid with 2 GHz spacing, all guard boundaries $f_{c_i} \pm (\Delta f_g + \delta_g)$, and the hardware-domain edges. With 100 GHz carrier spacing and a 50 GHz guard, the allowed interval between adjacent carriers reduces to a single point when $\delta_g = 0$ and disappears when $\delta_g > 0$. We use $\delta_g = 1$ GHz for the main results and compare it with clearances of 0, 2, 2.5, and 5 GHz. The 2.5 GHz clearance case is motivated by the ± 2.5 GHz frequency uncertainty specified for the EXFO FTBx-2850 tunable laser source[23]. All numerical optima are defined over the evaluated candidate set. At the 2, 3, 5 and 6 km operating points, the 2, 1 and 0.5 GHz grids gave the same wavelength selections and optimized yield bounds. Using 96 instead of 48 Gauss–Hermite points gave consistent results.

2.1.1 CSS Encoding and Three-Stage Protocol

A CSS code $[[n,k,d]]$ encodes the logical input state ρ_L into an n-qubit block. With encoding isometry V_Q, the encoded state is

$$\rho_{\mathrm{enc}} = V_Q \rho_L V_Q^{\dagger}. \tag{5}$$

An ideal recovery for the distance-d code corrects arbitrary errors supported on at most t physical-qubit locations, where

$$t = \left\lfloor \frac{d-1}{2} \right\rfloor. \tag{6}$$

For example, the Steane $[[7,1,3]]$ code encodes one logical qubit into seven physical qubits and admits an ideal recovery that corrects an arbitrary error acting on any one physical qubit. The protocol[19] requires three transmissions of the encoded quantum state over the same fiber span. We denote the wavelength-dependent physical channel associated with traversal (m) as follows,

$$\mathscr{E}_m(\lambda_q), \qquad m \in \{1,2,3\}. \tag{7}$$

The private transformations are assumed to act independently on the physical qubits,

$$U_A = \bigotimes_{j=1}^{n} A_j, \qquad U_B = \bigotimes_{j=1}^{n} B_j, \qquad [A_j, B_j] = 0. \tag{8}$$

Here A_j and B_j are single-qubit unitaries. The operations U_A, U_B, $U_A^{\dagger}$, and $U_B^{\dagger}$ are applied before traversals 1, 2, and 3, and before recovery, respectively. Their noiseless composition is $U_B^{\dagger} U_A^{\dagger} U_B U_A = I$. Encoding and recovery are ideal, and local private transformations preserve the support of physical errors.

2.2 Optical Impairments

Classical WDM propagation is treated under the undepleted-pump approximation. Fiber and optical-component parameters are modeled as deterministic wavelength-dependent functions under fixed operating conditions. Raman scattering, four-wave mixing, and finite-isolation leakage contribute additive optical background, whereas XPM is treated as differential polarization phase noise.

Let $\alpha_{\mathrm{dB}}(\lambda)$ denote the fiber attenuation coefficient in $\mathrm{dB\,km^{-1}}$. The corresponding attenuation coefficient in $\mathrm{m^{-1}}$ is

$$a(\lambda) = \frac{\ln 10}{10 \times 10^3}\,\alpha_{\mathrm{dB}}(\lambda). \tag{9}$$

The signal transmissivity during traversal m is

$$\eta_m(\lambda_q) = \eta_{\mathrm{ins},m}(\lambda_q)\,\eta_{\mathrm{mode},m}(\lambda_q)\,\exp[-a(\lambda_q)L_m], \tag{10}$$

where $\eta_{\mathrm{ins},m}$ includes the coupling and insertion losses between the specified input and output reference planes, and,

$$\eta_{\mathrm{mode},m}(\lambda_q) = \left| \int \psi_m^*(f)\, t_q(f; f_q)\, \psi_m(f)\, df \right|^2 \tag{11}$$

where T_q denotes the receiver filter's power response, with $t_q = \sqrt{T_q}$, and $\eta_{\mathrm{ins},m} = \eta_{\mathrm{tx},m}\eta_{\mathrm{rx},m}$ contains the launch and receive power transmissions. Background noise generated within the span reaches the output reference plane through $\eta_{\mathrm{rx},m}T_q$.

The accepted mode is assumed to be temporally aligned and matched to the deterministic propagation phase. Dispersion enters FWM phase matching and XPM walk-off, while residual signal dispersion and timing mismatch are excluded from the mode-overlap calculation. The total three-pass signal transmissivity is therefore,

$$T(\lambda_q) = \prod_{m=1}^{3} \eta_m(\lambda_q). \tag{12}$$

For $L_1 = L_2 = L_3 = L$,

$$T(\lambda_q) = \left[\prod_{m=1}^{3} \eta_{\mathrm{ins},m}(\lambda_q)\,\eta_{\mathrm{mode},m}(\lambda_q) \right] e^{-3a(\lambda_q)L}. \tag{13}$$

For traversal m, the polarization-summed additive background power at the output reference plane is

$$P^m_{\mathrm{add}}(\lambda_q) = P^m_{\mathrm{R}}(\lambda_q) + P^m_{\mathrm{FWM}}(\lambda_q) + P^m_{\mathrm{leak}}(\lambda_q). \tag{14}$$

1. **Spontaneous Raman scattering** $P_R^{(m)}(\lambda_q)$

   The signed frequency separation is

   $$\Delta f_{iq} = f_{c_i} - f_q, \tag{15}$$

   so positive and negative separations correspond to the Stokes and anti-Stokes sides, respectively. Let $\rho_R(\Delta f)$ denote the spontaneous Raman power coefficient, summed over the two receiver polarizations, in $\mathrm{m^{-1}\,Hz^{-1}}$.

   Use a longitudinal coordinate z measured from Alice toward Bob. For the nominal classical direction,

   $$P_{c_i}^{(m)}(z) = P_{c_i}^{(m)}(0)e^{-a_{c_i}z}, \qquad a_{c_i} = a(\lambda_{c_i}). \tag{16}$$

   The distance from a scattering point to the receiving terminal is $\ell_m(z) = L_m - z$ for reception at Bob and $\ell_m(z) = z$ for reception at Alice.

   The received Raman power spectral density is

   $$\begin{aligned} S^{(m)}_{\mathrm{R,out}}(f; f_q) = \eta_{\mathrm{rx},m}T_q(f; f_q) \sum_{i=1}^{N_c} \rho_R(f_{c_i} - f) \\ \times \int_0^{L_m} P_{c_i}^{(m)}(z) e^{-a(c/f)\ell_m(z)}\, dz. \end{aligned} \tag{17}$$

Here $\eta_{\mathrm{rx},m} T_q(f; f_q)$ is the power transmission from the fiber output to the selected output reference plane. The receive component loss and filter response are each applied once. For the finite modeled optical band $\mathscr{B}$,

$$P_{\mathrm{R}}^{(m)}(f_q) = \int_{\mathscr{B}} S_{\mathrm{R,out}}^{(m)}(f; f_q)\, df. \tag{18}$$

Raman noise is evaluated separately for each traversal. The closed-form co- and counter-propagating expressions are given in Supplementary Appendix A.1. The spectral shape of ρ_R follows the measured Raman gain spectrum of fused silica, $g_R(\Delta f)$[24], converted to spontaneous scattering with the Bose-Einstein occupation $n_{\mathrm{th}}(\Delta f)$: the Stokes and anti-Stokes sides scale as $g_R(\Delta f)[n_{\mathrm{th}}+1]$ and $g_R(|\Delta f|)\, n_{\mathrm{th}}$, respectively. The level is fixed by a measured coefficient in standard single-mode fiber[25], and a lower near-carrier measurement[26] is treated as a sensitivity case (Supplementary Appendix A.1).

2. **Four-wave mixing** $P_{\mathrm{FWM}}^{(m)}$

Classical channels at frequencies f_{c_i}, f_{c_j}, and f_{c_k} can generate a component at

$$f_{ijk} = f_{c_i} + f_{c_j} - f_{c_k}. \tag{19}$$

Let $\varsigma_i, \varsigma_j, \varsigma_k, \varsigma_g \in \{-1, +1\}$ specify propagation directions relative to the Alice-to-Bob coordinate. The longitudinal phase mismatch for an included mixing process is

$$\Delta\beta_{ijk}^{(m)} = \varsigma_i \beta(f_{c_i}) + \varsigma_j \beta(f_{c_j}) - \varsigma_k \beta(f_{c_k}) - \varsigma_g \beta(f_{ijk}). \tag{20}$$

Here $\beta(f)$ is the fiber propagation constant, and the signs $+1$ and -1 denote propagation toward Bob and Alice, respectively. Under the undepleted-pump approximation, with nonlinear contributions to the phase mismatch neglected, the directly received field amplitude is modeled as

$$A_{ijk}^{(m)} = i\, d_{ijk} \gamma_{ijk} \int_0^{L_m} \sqrt{P_{c_i}^{(m)}(z) P_{c_j}^{(m)}(z) P_{c_k}^{(m)}(z)} \times e^{i\Delta\beta_{ijk}^{(m)} z} e^{-a(c/f_{ijk})\ell_m(z)/2}\, dz. \tag{21}$$

The factors d_{ijk} and γ_{ijk} specify the permutation and effective polarization-coupling conventions. The amplitude $A_{ijk}^{(m)}$ is evaluated at the fiber output, before receiver component losses and filtering. The phase mismatch and propagation distance correspond to the generated-field direction. Reflected or back-scattered contributions require separate path terms. For the numerical simulations, pump pairs are enumerated as $i \le j$, with $k \notin \{i, j\}$. Using the conventional Kerr coefficient, the multiplicity is $d_{ijk} = 1$ for $i = j$ and $d_{ijk} = 2$ otherwise. Forward-generated FWM is collected during traversals 1 and 3, whereas backward and reflected contributions are excluded.

Let $g_{ijk}^{(m)}(f)$ be the normalized spectral power profile of a generated component, with $\int_{\mathscr{B}} g_{ijk}^{(m)}(f)\, df = 1$. Assuming mutually incoherent contributions from the included processes, the output power spectral density is

$$S_{\mathrm{FWM,out}}^{(m)}(f; f_q) = \eta_{\mathrm{rx},m} T_q(f; f_q) \sum_{(i,j,k)\in\mathscr{T}_m} |A_{ijk}^{(m)}|^2 g_{ijk}^{(m)}(f). \tag{22}$$

The admitted power is,

$$P_{\mathrm{FWM}}^{(m)}(f_q) = \int_{\mathscr{B}} S_{\mathrm{FWM,out}}^{(m)}(f; f_q)\, df. \tag{23}$$

For ideal monochromatic products, $g_{ijk}^{(m)}(f) = \delta(f - f_{ijk})$, giving

$$P_{\mathrm{FWM}}^{(m)}(f_q) = \eta_{\mathrm{rx},m} \sum_{(i,j,k)\in\mathscr{T}_m} |A_{ijk}^{(m)}|^2 T_q(f_{ijk}; f_q). \tag{24}$$

The generated frequencies are fixed by the classical deployment. Changing the quantum wavelength changes their overlap with the receiver response.

3. **Filter Leakage** ($P_{\mathrm{leak}}^{(m)}$).

Let $P_{c_i,\mathrm{rx}}^{(m)}$ denote classical power immediately before the receiver rejection response. Let,

$$P_{c_i,\mathrm{rx}}^{(m)} = P_{c_i,\mathrm{launch}}^{(m)} \tau_{i,m}, \tag{25}$$

where the dimensionless power transmission $\tau_{i,m}$ describes the optical path to that reference plane. For a remote transmitter whose signal traverses the span,

$$\tau_{i,m} = \tau_{i,m}^{\mathrm{up}} e^{-a_{c_i} L_m}, \tag{26}$$

Here $\tau_{i,m}^{\mathrm{up}}$ contains upstream component losses. For a local transmitter, $\tau_{i,m}$ instead describes the local coupling and isolation path.

Let $g_{c_i}^{(m)}(f)$ denote the normalized spectral power profile incident on the rejection chain, and let $T_{\mathrm{sys}}^{(m)}(f; f_q)$ denote its modeled power transmission to the quantum output reference plane. Then

$$S_{\mathrm{leak,out}}^{(m)}(f; f_q) = \sum_{i=1}^{N_c} P_{c_i,\mathrm{rx}}^{(m)} g_{c_i}^{(m)}(f) T_{\mathrm{sys}}^{(m)}(f; f_q), \tag{27}$$

and

$$P_{\mathrm{leak}}^{(m)}(f_q) = \int_{\mathscr{B}} S_{\mathrm{leak,out}}^{(m)}(f; f_q)\, df. \tag{28}$$

For a monochromatic classical channel, this reduces to

$$P_{\mathrm{leak}}^{(m)}(f_q) = \sum_{i=1}^{N_c} P_{c_i,\mathrm{rx}}^{(m)} T_{\mathrm{sys}}^{(m)}(f_{c_i}; f_q). \tag{29}$$

Losses included in $\tau_{i,m}$ are not applied again in $T_{\mathrm{sys}}^{(m)}$. The classical spectral profiles, including any assumed transmitter background, and the receiver rejection functions are specified as numerical model inputs.

4. **Cross-phase Modulation** ($p_{\mathrm{Z,XPM}}^{m}$)

The Kerr nonlinear coefficient at the quantum wavelength is,

$$\gamma(\lambda_q) = \frac{2\pi n_2(\lambda_q)}{\lambda_q A_{\mathrm{eff}}(\lambda_q)}, \tag{30}$$

where n_2 is the nonlinear refractive-index coefficient and A_{eff} is the effective mode area. For a polarization-encoded qubit, only a differential phase between the two logical components changes the quantum state. A common phase is global and thus has no observable effect. Let

$$\Delta\phi_m(t) = \phi_{H,m}(t) - \phi_{V,m}(t) \tag{31}$$

denote the differential XPM phase during traversal m. We model this phase as

$$\Delta\phi_m(t) = 2\sum_{i=1}^{N_c} \gamma_{iq}(\lambda_q)\kappa_{i,m} \int_0^{L_m} P_{c_i}^{(m)}\left(z, t - \tau_{iq}^{(m)}(z)\right) dz, \tag{32}$$

where $\gamma_{iq}(\lambda_q)$ is the effective cross-nonlinearity coefficient, $\kappa_{i,m}$ characterizes differential polarization coupling, and $\tau_{iq}^{(m)}(z)$ denotes the relative group-delay or walk-off function for the propagation configuration used during traversal m. We assume that the deterministic mean differential phase has been compensated. The residual fluctuation is

$$\delta\phi_m = \Delta\phi_m - \mathbb{E}[\Delta\phi_m]. \tag{33}$$

Within the selected-mode approximation, the residual differential phase is constant over each quantum pulse, with variance $\sigma_{\phi,m}^2 = \mathrm{Var}(\delta\phi_m)$. Supplementary Appendix A.2 derives the variance and phase autocovariance from the classical intensity fluctuations.

The corresponding polarization coherence factor is

$$C_m = \mathbb{E}\left[e^{-i\delta\phi_m}\right]. \tag{34}$$

For zero-mean Gaussian residual phase fluctuations, $C_m = \exp\left(-\sigma_{\phi,m}^2/2\right)$. The resulting dephasing channel is equivalent to applying a Pauli Z operation with probability

$$p_{\mathrm{Z,XPM}}^{m} = \frac{1 - C_m}{2} \tag{35}$$

If both polarization components acquire the same phase, the differential phase vanishes, giving $\sigma_{\phi,m}^2 = 0$ and $p_{\mathrm{Z,XPM}}^{m} = 0$.

2.3 Quantum Channel Model

The optical impairments defined above are mapped to a qubit channel through a specified receiver acceptance operation. Each physical qubit occupies a selected spatial and temporal mode with two orthogonal polarization components. The optical encoding isometry W is defined by

$$W|0\rangle = |1_H, 0_V\rangle, \qquad W|1\rangle = |0_H, 1_V\rangle. \tag{36}$$

After traversal 3, the receiver applies an ideal nondestructive one-photon projection, $\Pi_1 = WW^\dagger$. Block acceptance requires one photon in all n modes, with no intermediate photon-number post-selection. Private transformations and stochastic polarization operations preserve the selected spatial and temporal mode and extend to passive, photon-number-preserving operations on the full two-polarization optical space, with the stated qubit operations as their one-photon restrictions. Attenuation is polarization-independent. We model the additive background as zero-mean, phase-insensitive Gaussian noise with identical independent contributions in the two polarization modes. The vacuum-input background in each selected polarization mode is therefore thermal. This approximation represents an incoherent background formed from many independent contributions. Its application to FWM and leakage is an additional modeling assumption, since their estimated powers do not determine their photon statistics or field coherence.

Error realizations are assumed independent across physical-qubit modes and traversals. For temporally multiplexed qubits, pulse spacing must suppress mode overlap and received-background and XPM correlations. Mode orthogonality alone does not establish noise independence. We report yield per encoded block without assigning a pulse repetition rate.

The polarization-summed background spectral density used in the optical-to-qubit reduction is

$$S^{(m)}_{\mathrm{add,out}} = S^{(m)}_{\mathrm{R,out}} + S^{(m)}_{\mathrm{FWM,out}} + S^{(m)}_{\mathrm{leak,out}}. \tag{37}$$

The spectral densities are evaluated before integrating over optical frequency. Their integrated powers alone do not determine occupancy of a specified temporal mode.

Let $\nu_m(\lambda_q)$ denote the background occupancy added per polarization mode at the output of traversal m for vacuum input. For a stationary background, the accepted-mode occupancy[25] is

$$\nu_m(\lambda_q) = \frac{1}{2}\int_0^\infty |\psi_m(f)|^2 \frac{S^{(m)}_{\mathrm{add,out}}(f;\lambda_q)}{hf}\, df, \tag{38}$$

where $S^{(m)}_{\mathrm{add,out}}$ is the polarization-summed output power spectral density, h is Planck's constant, and $\int_0^\infty |\psi_m(f)|^2 df = 1$. The factor $1/2$ assigns equal occupancy to both polarizations. Signal transmission and background are evaluated at consistent optical reference planes, including the relevant filtering and coupling losses. The scalar composition assumes that each terminal retains the selected mode, discards orthogonal modes, and relaunches the retained field in the mode specified for the next traversal.

With independent backgrounds and wavelength arguments suppressed, the final occupancy is

$$\nu = \eta_3\eta_2\nu_1 + \eta_3\nu_2 + \nu_3. \tag{39}$$

The reported scans and certificates use this ν and $T = \prod_{m=1}^3 \eta_m$ from Equation (12). The full-chain quantities T_{ref} and ν_{ref} in Supplementary Appendix A.3 are used for receiver-model comparisons.

Identical thermal channels on both polarizations are covariant under polarization rotations. Their composition gives the unnormalized accepted operation[27],

$$\mathscr{M}_{\mathrm{opt}}(\rho) = c_0\rho + c_1\frac{I_2}{2}\mathrm{Tr}\,\rho, \tag{40}$$

where

$$c_0 = \frac{T}{(1+\nu)^4}, \qquad c_1 = \frac{2\nu(1+\nu-T)}{(1+\nu)^4}. \tag{41}$$

The coefficients and state-independent acceptance probability are derived in Supplementary Appendix B.

For a normalized input state, the acceptance probability is $s = c_0 + c_1$, independently of the input polarization. For $s > 0$, the conditional optical qubit channel is,

$$\Lambda_{\mathrm{opt}}(\rho) = (1-r)\rho + r\frac{I_2}{2}, \qquad r = \frac{c_1}{s}. \tag{42}$$

Its Pauli representation has probabilities

$$w_I = 1 - \frac{3r}{4}, \qquad w_X = w_Y = w_Z = \frac{r}{4}. \tag{43}$$

When $\nu = 0$ and $T > 0$, the optical model gives $s = T$ and $r = 0$. When $T = 0$ and $\nu > 0$, the accepted output is maximally mixed. At $T = \nu = 0$, acceptance has zero probability, and the conditional channel is undefined. Acceptance must therefore be distinguished from preservation of the input quantum state.

Base imperfections and residual differential XPM phase noise are modeled separately from the additive optical background. Let $a_{0,m} = e_{0,m}/2$, where $e_{0,m}$ is the base conditional basis-error probability and $0 \le a_{0,m} \le 1/3$. The base channel has Pauli probabilities $(1-3a_{0,m}, a_{0,m}, a_{0,m}, a_{0,m})$. Let $z_m = p^m_{\mathrm{Z,XPM}}$ denote the phase-flip probability defined above. The identity probability of the composed base and XPM channels is

$$b_m = (1-z_m)(1-3a_{0,m}) + z_m a_{0,m}. \tag{44}$$

The second term accounts for cancellation when both channels apply Z. The base error $e_{0,m}$ includes residual polarization misalignment, preparation and analysis errors, and imperfect private rotations, excluding background already included in Λ_{opt}. We use $e_{0,m} = 0.2\%$ and test each operating point at published basis-error rates: 0.07% for a self-compensating encoder[28], about 0.4% for a GHz-rate system[29], and 0.7–1.8% for a compensated 16 km link[30]. The maximum admissible base error is defined in Eq. (58).

Assuming independence of the optical background, base errors, and XPM contributions, and independence of error realizations across traversals, define

$$q = 1 - w_I \prod_{m=1}^{3} b_m. \tag{45}$$

This is the probability that a physical-qubit location contains at least one nonidentity event in the adopted stochastic representation. It counts affected locations without relying on cancellation between errors occurring during different traversals.

Under the local private-operation assumptions stated above, an error history affecting at most $t = \lfloor (d-1)/2 \rfloor$ locations remains supported on at most t physical qubits. An ideal recovery for the distance-d code corrects all such errors[31]. For independent physical-qubit modes with identical channel parameters, the guaranteed correctable-history weight is

$$C_{n,t}(q) = \sum_{\ell=0}^{t} \binom{n}{\ell} q^{\ell} (1-q)^{n-\ell}. \tag{46}$$

Histories affecting more than t locations are excluded from this guarantee, although some may also be corrected. For the Steane $[[7,1,3]]$ code,

$$C_{7,1}(q) = (1-q)^7 + 7q(1-q)^6. \tag{47}$$

State-independent single-mode acceptance and independence of the optical channels give $P_{\mathrm{acc}} = s^n$. This holds for entangled encoded inputs as well as product inputs. For fixed admissible private transformations, let Λ_L denote the decoded logical channel conditioned on block acceptance. Its entanglement fidelity is

$$F_e(\Lambda_L) = \langle \Phi_k | (\mathrm{id}_R \otimes \Lambda_L)(|\Phi_k\rangle\langle\Phi_k|) |\Phi_k\rangle, \tag{48}$$

Here $|\Phi_k\rangle$ is a normalized maximally entangled state of the k logical qubits and a k-qubit reference system R. Conditioned on block acceptance, guaranteed correctable histories have total probability $C = C_{n,t}(q)$ and induce the identity logical channel after recovery. For $C < 1$, the remaining histories define a completely positive trace-preserving channel $\mathscr{B}_L$, giving

$$\Lambda_L = C\,\mathrm{id}_L + (1-C)\mathscr{B}_L. \tag{49}$$

Entanglement fidelity is affine in the channel, giving

$$F_e(\Lambda_L) = C + (1-C)F_e(\mathscr{B}_L) \ge C_{n,t}(q). \tag{50}$$

The inequality follows from $F_e(\mathscr{B}_L) \ge 0$. For $C = 1$, recovery gives the identity logical channel. We define the unconditional entanglement-fidelity yield as

$$Y = P_{\mathrm{acc}} F_e(\Lambda_L). \tag{51}$$

The lower and upper yield bounds are,

$$Y_{\mathrm{lb}}(\lambda_q) = s(\lambda_q)^n C_{n,t}(q(\lambda_q))\,, \text{ and } Y_{\mathrm{ub}}(\lambda_q) = s(\lambda_q)^n. \tag{52}$$

Therefore,

$$Y_{\mathrm{lb}}(\lambda_q) \le Y(\lambda_q) \le Y_{\mathrm{ub}}(\lambda_q). \tag{53}$$

The lower bound is the accepted weight of guaranteed correctable histories, while the upper bound follows from $F_e(\Lambda_L) \le 1$. We do not assume that recovery indicates when correction has succeeded. The definitions below apply to the full admissible wavelength domain Ω_q. In the numerical evaluations in Sec. 3, we restrict the search to the finite candidate set $\Omega_q^{\mathrm{eval}}(\delta_g)$. All numerical maxima and feasibility classifications refer to this evaluated set.

For a required minimum conditional fidelity $F_{\min} \in (0,1]$, define the wavelength domain satisfying the fidelity certificate,

$$\Omega_F = \left\{\lambda_q \in \Omega_q : s(\lambda_q) > 0,\, C_{n,t}(q(\lambda_q)) \ge F_{\min}\right\}. \tag{54}$$

The wavelength-selection objective is

$$\lambda_q^\star \in \underset{\lambda_q \in \Omega_F}{\arg\max}\, Y_{\mathrm{lb}}(\lambda_q), \tag{55}$$

provided that Ω_F is nonempty and the maximum is attained. Attainment is automatic for a nonempty finite evaluated candidate set. For a required minimum yield $Y_{\min} > 0$, the certified operating region is

$$\mathscr{W}_q(Y_{\min}, F_{\min}) = \left\{\lambda_q \in \Omega_F : Y_{\mathrm{lb}}(\lambda_q) \ge Y_{\min}\right\}. \tag{56}$$

Membership in $\mathscr{W}_q$ certifies both requirements under the stated model. Failure to satisfy a lower-bound condition does not establish physical infeasibility. In contrast, $Y_{\mathrm{ub}}(\lambda_q) < Y_{\min}$ excludes a wavelength from meeting the yield requirement for the specified acceptance architecture. The optimization maximizes the established guarantee and need not maximize the exact fidelity yield.

For a prescribed relative tolerance $\varepsilon \in [0,1)$, the near-optimal wavelength region is

$$\mathscr{N}_\varepsilon = \left\{\lambda_q \in \Omega_F : Y_{\mathrm{lb}}(\lambda_q) \ge (1-\varepsilon) Y_{\mathrm{lb}}(\lambda_q^\star)\right\}. \tag{57}$$

For comparison, we also maximize T and minimize q over the evaluated allowed domain and its fidelity-certified subset. Each selected wavelength is evaluated using the same optical and logical channel, with its fidelity and yield certification reported separately. Let $q(\lambda_q; e_0)$ denote Eq. (45) with $e_{0,m} = e_0$ for all three traversals. At each operating point, the maximum admissible base error is

$$e_0^{\max} = \max\left\{e_0 \in [0, 2/3] : \exists \lambda_q \in \Omega_q \text{ with } s(\lambda_q) > 0,\, C_{n,t}(q(\lambda_q; e_0)) \ge F_{\min}\right\}. \tag{58}$$

Since q increases with e_0 for $z_m < 3/4$, we compute $e_0^{\max}$ by bisection. If no candidate is certified at $e_0 = 0$, no base error is admissible.

An admissible operating point satisfies the classical link budget and admits a wavelength meeting both quantum thresholds,

$$\mathscr{R}(Y_{\min}, F_{\min}) = \left\{(L, P_c) : P_c \ge P_{c,\min}(L),\, \mathscr{W}_q(Y_{\min}, F_{\min}) \ne \emptyset\right\}, \tag{59}$$

where $\mathscr{W}_q$ is evaluated at (L, P_c). We report results along $P_c = P_{c,\min}(L)$ and over the distance-power map.

3 Results

We evaluated the Steane $[[7,1,3]]$ code with fixed CSS Hamming recovery using $F_{\min} = 0.99$ and $Y_{\min} = 10^{-6}$. Unless varied, the base error was $e_{0,m} = 0.2\%$ for all three traversals. Distances refer to one traversal and classical launch powers to one channel. Signal transmission and background occupancy were evaluated for the same selected spectral mode. The fiber, filter, receiver, base-error, and XPM parameters, together with their sources and coupling conventions, are listed in Table 1.

Four different operating points were used to compare wavelength selection at different distances and launch powers: 2 km/−15 dBm, 3 km/−13 dBm, 5 km/−10 dBm, and 10 km/−5 dBm. We calculated the logical entanglement fidelity for identity private transformations at each allowed candidate wavelength in these scans. We compared the results with the key-independent certificate $C_{7,1}(q)$ and the yield bounds derived in Sec 2.

Table 1. Baseline physical parameters for the fiber-coexistence simulations. Additional spectral and sensitivity settings are specified in Supplementary Appendix A.4 and in the released code.

Parameter	Value or model
Fiber response	Attenuation interpolation anchored to SMF-28 Ultra specifications: $\alpha(1550\,\mathrm{nm}) = 0.180$ dB km^{-1}, with interpolated values of 0.188 and 0.183 dB km^{-1} at 1530 and 1565 nm, respectively. $\beta_2 = -2.17 \times 10^{-26}$ s^2 m^{-1}, $\beta_3 = 1.2 \times 10^{-40}$ s^3 m^{-1}, $n_g = 1.468$
Kerr coefficient	$\gamma = 1.3$ W^{-1} km^{-1}
Raman background	$\rho = 2.85 \times 10^{-9}$ km^{-1} nm^{-1} at pump/observation 1559.79/1554.94 nm ($\Delta f = -0.599$ THz)[25], equivalent to $\rho_f = 2.30 \times 10^{-23}$ m^{-1} Hz^{-1}. Hollenbeck-Cantrell fit to measured silica Raman gain[24], with Bose factor at 300 K. Near-carrier level from[26] used as a sensitivity case
Optical mode	Normalized Gaussian spectral intensity $\lvert\psi(f)\rvert^2$, 10 GHz intensity FWHM
Receiver filter	Super-Gaussian power response, $m = 4$, 25 GHz FWHM, transmission floor 10^{-11} (-110 dB), modeled over 1500–1600 nm
Component transmission	$\eta_{\mathrm{ins}} = 0.82$ per traversal, with power transmissions $\sqrt{0.82}$ at the launch and receive planes
Leakage	Isolation 110 dB (remote) and 90 dB (local). Broadband background 2.5×10^{-14} Hz^{-1} of carrier power, carrier width 25 GHz rms
Base error	Nominal $e_{0,m} = 0.002$ for $m = 1,2,3$. Comparison values span 0.07–1.8% [28–30]
Classical link budget	$S_{\mathrm{rx}} = -36.8$ dBm at 1.25 Gb/s[11], and assumed -24 dBm benchmark at 10.7 Gb/s. $IL_{\mathrm{demux}} = 3$ dB, $M_{\mathrm{sys}} = 3$ dB, $\alpha_c = 0.188$ dB km^{-1}
XPM	$\kappa = 1.0$, relative intensity fluctuation 100% rms, flat two-sided PSD over $\lvert F\rvert \le 25$ GHz, with co- and counter-propagating walk-off

The attenuation interpolation, dispersion, group index, Kerr coefficient, component losses, leakage, nominal base error, link-budget losses and margin, and XPM settings are assumed. The Raman calibration and shape, base-error comparison values, and 1.25 Gb/s receiver sensitivity are based on the cited sources. The 10.7 Gb/s sensitivity is an assumed benchmark.

Component transmission excludes span attenuation and filter-induced modal transmission. Isolation excludes the quantum filter. Base error excludes additive optical background.

Classical powers are specified at the fiber input. The classical budget includes a 3 dB demultiplexer loss and a 3 dB system margin. Input multiplexer loss determines the required upstream transmitter power and is excluded from the fiber-input budget.

3.1 Optical Channel and Logical Fidelity Evaluation

Figure 1 compares the analytical accepted optical channel with an independent numerical model of the signal interacting with a thermal environment. The calculations match for both the acceptance probability (s) and the conditional mixing parameter (r) over the tested transmissivities and background occupancies. Subfigure (a) illustrates the distinction between detecting an accepted optical state and preserving an input qubit state. At low transmissivity, increasing background occupancy can increase s, because background photons contribute to accepted one-photon outcomes. The simultaneous increase in r shows that these additional accepted events do not imply improved preservation of the input polarization state.

To compare the accepted operations themselves, we used their Choi operators, obtained by applying each operation to one half of a normalized maximally entangled state. The trace of each operator equals the acceptance probability. At the numerical cutoffs marked by stars in Figure 1(c), the trace-norm difference between the operators is of order 10^{-16}–10^{-15}, below the 10^{-9} target. The explicit three-traversal channel and its effective composition also agree within 10^{-15}. At selected diagnostic candidates for the four operating points, the full-chain calculation differs from the scalar composition by at most 0.6% in T, 0.4% in ν, and 4.5% in Y_{lb} (Supplementary Figure S1(b)). The factor s^7 amplifies small acceptance differences. The wavelength scans and operating maps use the scalar composition for fidelity certificates and yield bounds. The full-chain calculation serves as a diagnostic check.

We then evaluated the logical entanglement fidelity after ideal Steane recovery. Figure 2 compares the calculated fidelity with the certificate $C_{7,1}(q)$. For identity private transformation, calculating recovery directly from the density matrix and enumerating the Pauli error patterns gave results agreeing to approximately 10^{-13}. The calculated infidelity remains below $1 - C_{7,1}(q)$ for the tested identity and non-Clifford transformations. At small q, infidelity grows approximately as q^2, consistent with the correction of errors affecting a single location.

The gap between fidelity and the certificate grows with q and is larger for the XPM-dominated synthetic noise path (Figure 2(b)). This path also produces a larger fidelity spread over the 16 sampled random key sets and larger differences between fixed and identity keys (Figure 2(c)). The two paths differ in background occupancy and base error as well as XPM variance, so this comparison does not isolate the effect of XPM alone. These comparisons describe the tested keys, while wavelength certification uses the key-independent lower bound $C_{7,1}(q)$.

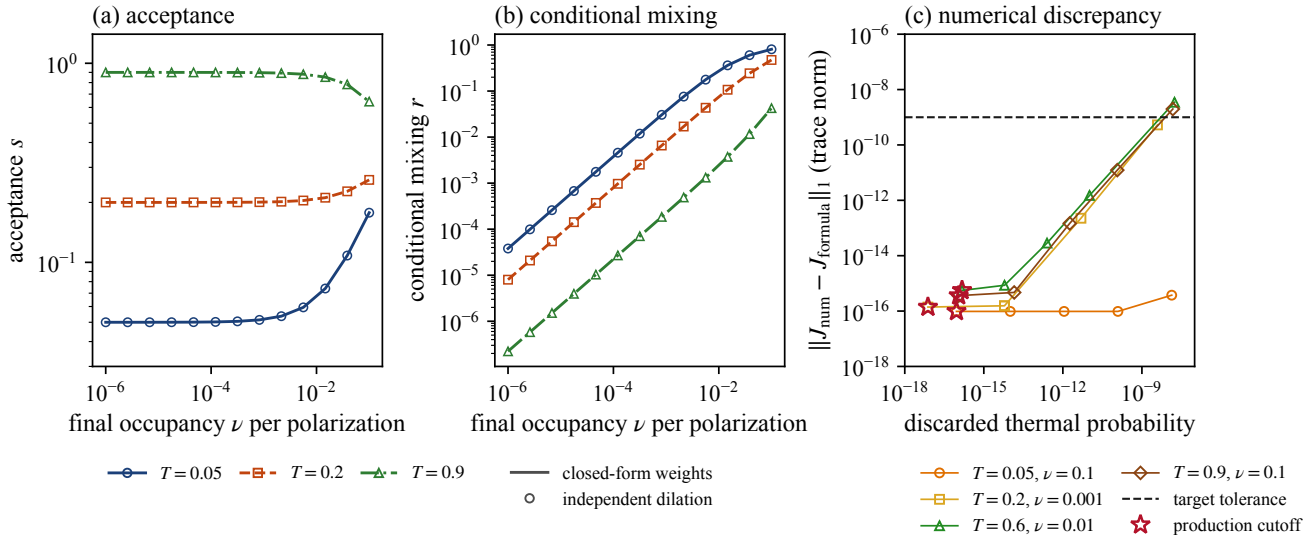

Figure 1. Verification of the accepted optical channel. (a) Acceptance probability s and (b) conditional mixing r vs background occupancy ν per polarization. Lines show the analytical model and symbols the independent thermal dilation. (c) Choi-operator discrepancy versus discarded thermal probability.

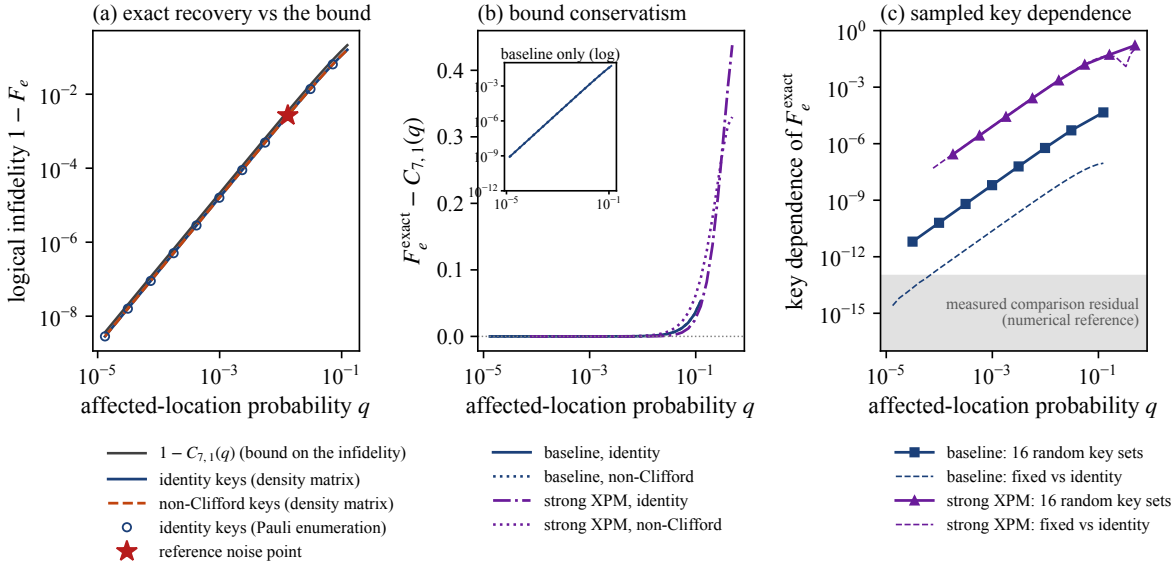

Figure 2. Logical fidelity after Steane code recovery. (a) Calculated infidelity and the bound $1 - C_{7,1}(q)$. (b) Gap between fidelity and the certificate for baseline and strong-XPM noise. (c) Fidelity spread over 16 random key sets and fixed-versus-identity key comparisons.

3.2 Wavelength Selection

Figure 3 shows the wavelength scan at 5 km per traversal and −10 dBm per classical channel. Raman scattering dominates the broad background, whereas narrow FWM peaks produce localized dips in fidelity. Leakage remains well below the Raman contribution. All three wavelength windows satisfy $F_{\min} = 0.99$ and $Y_{\min} = 10^{-6}$ at this operating point.

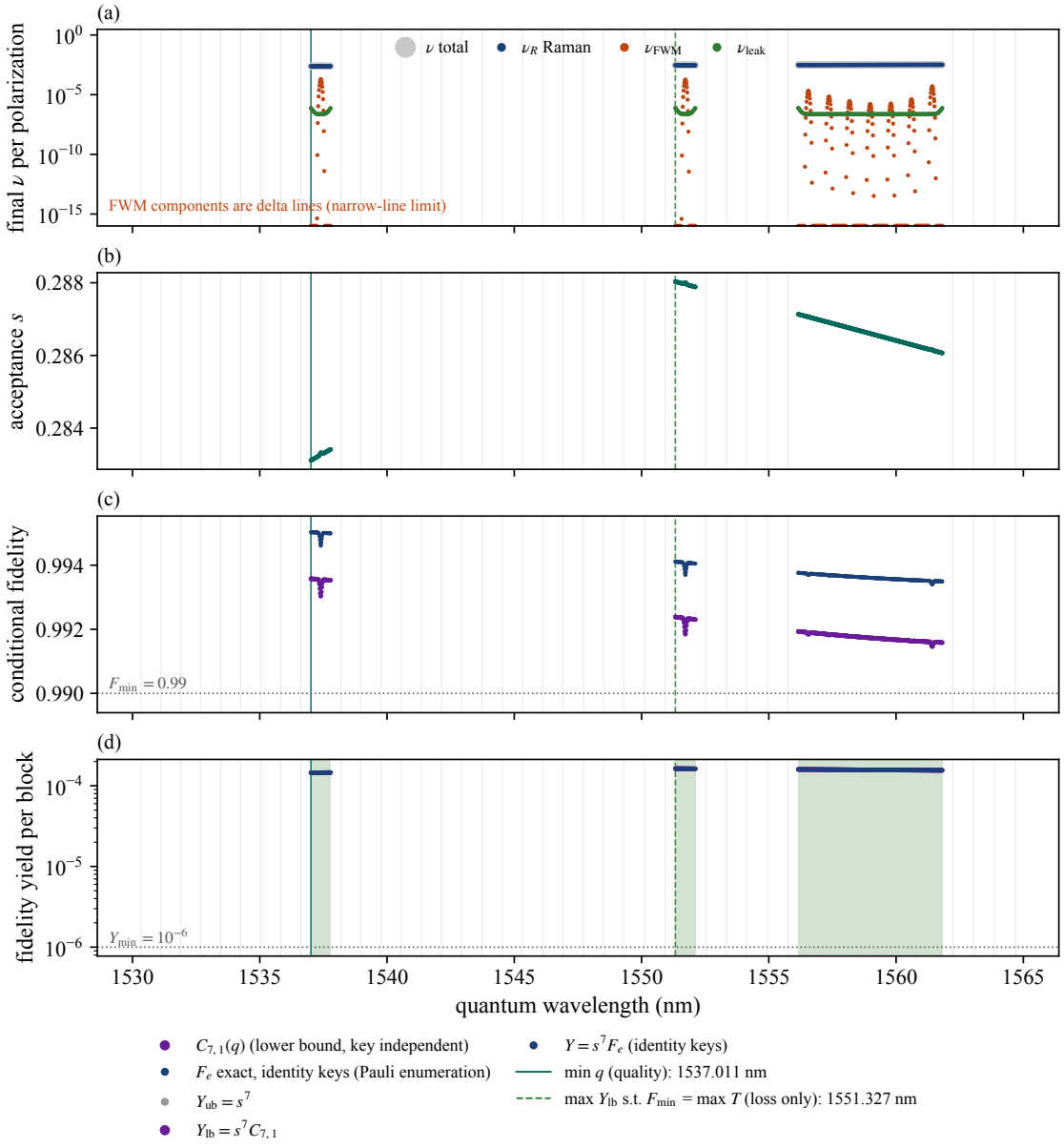

Figure 3. Wavelength selection at 5 km per traversal and −10 dBm per classical channel. (a) Background contributions, (b) acceptance probability, (c) logical fidelity and certificate, and (d) fidelity yield and its bounds. Shading marks admissible windows. Vertical lines mark the minimum-q and maximum-Y_{lb} choices. The latter coincides with the loss-only choice. FWM uses the narrow-line limit.

Minimizing q selects 1537.011 nm, whereas maximizing Y_{lb} subject to the fidelity threshold selects 1551.327 nm. The latter also coincides with the maximum-transmission choice. Its higher acceptance outweighs its lower fidelity certificate in $Y_{\text{lb}} = s^7 C_{7,1}(q)$. The wavelength with the largest certificate therefore differs from the wavelength with the largest yield bound at this operating point.

Table 2 compares the fidelity-constrained maximizer of Y_{lb} with the maximum-transmission and minimum-q selections. At 6 km and −10 dBm per channel, unconstrained transmission maximization selects a wavelength that does not satisfy the fidelity

Table 2. Comparison of wavelength-selection rules, including a point near the fidelity boundary.

L (km)	P_c (dBm)	Selection	λ_q (nm)	$C_{7,1}(q)$	Y_{lb}	Certified
2	−15	Max. Y_{lb} / max. T	1551.327	0.99800	2.191×10^{-3}	Yes
		Min. q	1537.011	0.99806	2.091×10^{-3}	Yes
3	−13	Max. Y_{lb} / max. T	1551.327	0.99730	9.157×10^{-4}	Yes
		Min. q	1537.011	0.99748	8.535×10^{-4}	Yes
5	−10	Max. Y_{lb} / max. T	1551.327	0.99238	1.632×10^{-4}	Yes
		Min. q	1537.011	0.99358	1.448×10^{-4}	Yes
6	−10	Max. Y_{lb}	1537.784	0.99133	6.077×10^{-5}	Yes
		Max. T	1551.327	0.98962	6.967×10^{-5}	No
		Min. q	1537.011	0.99140	6.023×10^{-5}	Yes
10	−5	Max. Y_{lb}	—	—	—	—
		Max. T	1551.327	0.83982	3.137×10^{-6}	No
		Min. q	1537.011	0.87077	2.391×10^{-6}	No

Maximization of Y_{lb} uses the evaluated fidelity-certified candidates. Maximum T and minimum q use the full evaluated allowed domain. Certification requires $C_{7,1}(q) \geq 0.99$ and $Y_{\mathrm{lb}} \geq 10^{-6}$. "No" means that these bounds do not certify both requirements; it does not establish failure of the exact logical fidelity. All rows use $e_{0,m} = 0.2\%$ and $\delta_g = 1$ GHz.

Restricting the baselines to fidelity-certified candidates leaves their selections unchanged except for maximum T at 6 km/−10 dBm, which selects 1537.784 nm. At 10 km/−5 dBm, no candidate is fidelity-certified, so the constrained selections are undefined.

certificate. Restricting transmission maximization to fidelity-certified candidates recovers the same wavelength as maximizing Y_{lb}. This comparison illustrates the role of the fidelity constraint; it does not demonstrate an advantage over the constrained transmission baseline.

3.3 Operating Regions and Sensitivity

Figure 4(a) shows the optimized yield bound over distance and classical launch power. Increasing either distance or power reduces the fidelity-certified region, while the yield falls sharply with distance within that region. Admissible operating points must also meet the yield threshold and provide sufficient received power for classical communication. The 10.7 Gb/s link-budget curve leaves the fidelity-certified region at a shorter span than the 1.25 Gb/s curve because it requires higher launch power. The selected wavelength stays near 1551 nm over most certified points and switches to the window near 1537 nm close to the fidelity boundary (Figure 4(b)).

At 3 km/−13 dBm and 5 km/−10 dBm, adding 1 GHz of tuning clearance shifts the selected wavelength by about 0.8 nm. Increasing the clearance to 5 GHz reduces the optimized yield bound by less than 0.5% relative to zero clearance (Figure 4(c)). Thus, changing the selected wavelength incurs only a small yield penalty at these two operating points.

At the reference point, doubling either the Raman level or the base error removes all fidelity-certified candidates (Figure 4(d)). For the alternative Raman shape A, the nominal wavelength no longer meets the fidelity-certification threshold, but selecting another wavelength restores certification. FWM profile widths of 1, 5 and 25 GHz rms, a tenfold increase in transmitter background, and a 10 dB reduction in isolation retain certification at this operating point. Broader FWM profiles reduce peak occupancy across the four operating points.

The admissible base error approaches 0.5% at short spans and low launch powers, and decreases with distance and power, more quickly along the 10.7 Gb/s link budget. Values of 0.07% and about 0.4% are admissible over part of the scan, while $0.7 - 1.8\%$ exceeds the limit throughout. Along the 1.25 Gb/s link-budget curve at $e_0 = 0.2\%$, the optimized yield bound crosses 10^{-6} between 10 and 11 km per traversal, while fidelity remains certified through the largest evaluated distance of 30 km. For the assumed 10.7 Gb/s receiver benchmark, fidelity remains certified through 13 km on the evaluated distance grid, whereas both thresholds are met only through 10 km.

4 Discussion

Quantum-augmented networks (QuANets) integrate selected quantum devices and protocols with classical network infrastructure to support communication and security functions. Sharing fiber between these services requires sufficient classical launch power for data reception while limiting the background introduced at the quantum receiver. For protocols involving repeated traversals, loss and noise accumulate before logical recovery, further restricting operation. This work identifies the distances,

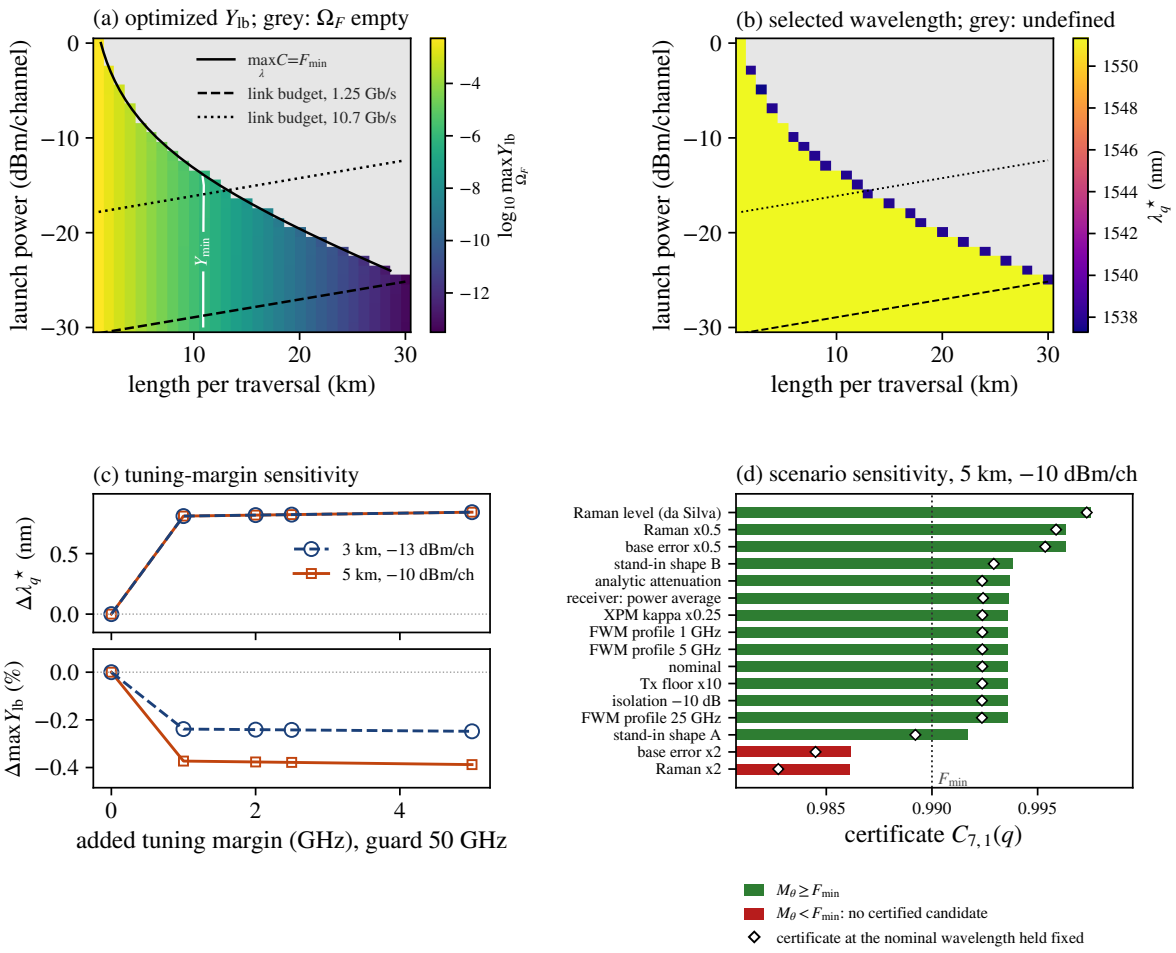

Figure 4. Operating regions and sensitivity. (a) Optimized yield bound and (b) selected wavelength, with classical link-budget minima. Grey regions have no fidelity-certified candidate. (c) Effect of tuning clearance. (d) Maximum certificate over wavelength (bars) and certificate at the fixed nominal wavelength (diamonds) under parameter variations at 5 km and −10 dBm per channel.

launch powers, and wavelengths that satisfy the classical link budget and certify the required quantum fidelity and yield under the assumed coexistence model.

The results show that logical fidelity and block yield impose different limits on coexistence. At 5 km per traversal and -10 dBm per classical channel, the largest fidelity certificate occurs at 1537.011 nm, while the largest yield bound among fidelity-certified candidates occurs at 1551.327 nm. Along the 1.25 Gb/s link-budget minimum at $e_0 = 0.2\%$, the yield bound falls below 10^{-6} between 10 and 11 km per traversal, while fidelity remains certified at longer spans. The yield requirement therefore limits certified operation before the fidelity requirement in this case.

A QuANet gateway could use these criteria to assess whether a proposed quantum transmission meets its fidelity and yield requirements. The key-independent certificate allows this assessment without knowing the private transformation keys. It provides a sufficient condition for logical-state preservation under the assumed noise model. Failure of certification does not establish failure for every key. Confidentiality, authentication, and anonymity still require protocol-level security analyses.

The wavelength choices obtained here depend on the classical carrier deployment and hardware assumptions. At the reference point, doubling either the Raman level or the base error removes all fidelity-certified candidates, making calibration necessary for practical wavelength selection. The thermal approximation and the assumed independence of physical-qubit modes require experimental validation through measurements of photon statistics and temporal noise correlations. Future evaluations should include receiver and recovery errors, validate mode restoration, and account for changing classical traffic and wavelength availability. These extensions could allow a quantum gateway to update its wavelength choice as link conditions change.

References

1. Berrevoets, R. C. *et al.* Deployed measurement-device independent quantum key distribution and bell-state measurements coexisting with standard internet data and networking equipment. *Commun. Phys.* **5**, 186 (2022).
2. Alia, O. *et al.* Dynamic dv-qkd networking in trusted-node-free software-defined optical networks. *J. Light. Technol.* **40**, 5816–5824 (2022).
3. Burenkov, I. A. *et al.* Synchronization and coexistence in quantum networks. *Opt. Express* **31**, 11431–11446 (2023).
4. Martin, V. *et al.* Madqci: a heterogeneous and scalable sdn-qkd network deployed in production facilities. *npj Quantum Inf.* **10**, 80 (2024).
5. Wang, R. *et al.* Field trial of a dynamically switched quantum network supporting co-existence of entanglement, prepare-and-measure qkd and classical channels. In *IET Conference Proceedings CP839*, vol. 2023, 1682–1685 (IET, 2023).
6. Rahmouni, A. *et al.* 100-km entanglement distribution with coexisting quantum and classical signals in a single fiber. *J. Opt. Commun. Netw.* **16**, 781–787 (2024).
7. Jha, N., Parakh, A. & Subramanian, M. A ml based approach to quantum augmented http protocol. In *2024 IEEE International Conference on Quantum Computing and Engineering (QCE)*, vol. 2, 591–592 (IEEE, 2024).
8. Jha, N., Parakh, A. & Subramaniam, M. Towards a quantum-classical augmented network. In *Quantum Computing, Communication, and Simulation V*, vol. 13391, 72–86 (SPIE, 2025).
9. Jha, N., Parakh, A. & Subramaniam, M. An improved quantum anonymous notification protocol for quantum-augmented networks. *Front. Quantum Sci. Technol.* **5**, 1704298 (2026).
10. Jha, N., Parakh, A. & Subramaniam, M. Quantum key distribution: Bridging theoretical security proofs, practical attacks, and error correction for quantum-augmented networks. *Cryptologia* 1–58, DOI: 10.1080/01611194.2025.2596885 (2026).
11. Patel, K. *et al.* Coexistence of high-bit-rate quantum key distribution and data on optical fiber. *Phys. Rev. X* **2**, 041010 (2012).
12. Patel, K. *et al.* Quantum key distribution for 10 gb/s dense wavelength division multiplexing networks. *Appl. Phys. Lett.* **104**, DOI: 10.1063/1.4864398 (2014).
13. Eriksson, T. A. *et al.* Wavelength division multiplexing of continuous variable quantum key distribution and 18.3 tbit/s data channels. *Commun. Phys.* **2**, 9 (2019).
14. Wu, Q. *et al.* Integration of quantum key distribution and high-throughput classical communications in field-deployed multi-core fibers. *Light. Sci. & Appl.* **14**, 274 (2025).
15. Kong, W. *et al.* Enhanced coexistence of quantum key distribution and classical communication over hollow-core and multi-core fibers. *Entropy* **26**, 601 (2024).

16. Ding, Y., Bi, L. & Verma, G. Channel-aware dynamic routing for optimizing coexistence of quantum and classical channels in dwdm networks. *Opt. Fiber Technol.* **99**, 104591 (2026).

17. Bahrani, S., Razavi, M. & Salehi, J. A. Wavelength assignment in hybrid quantum-classical networks. *Sci. reports* **8**, 3456 (2018).

18. Zischler, L. A., Ghazisaeidi, A., Mecozzi, A. & Antonelli, C. Secret key rate limits in coexisting classical-quantum optical links. *arXiv preprint arXiv:2602.21671* (2026).

19. Kak, S. A three-stage quantum cryptography protocol. *Foundations Phys. Lett.* **19**, 293–296 (2006).

20. Jha, N., Parakh, A. & Subramaniam, M. Joint encryption and error correction for secure quantum communication. *Sci. Reports* **14**, 24542 (2024).

21. Mandal, S. *et al.* Multi-photon implementation of three-stage quantum cryptography protocol. In *The International Conference on Information Networking 2013 (ICOIN)*, 6–11 (IEEE, 2013).

22. Wu, L. & Chen, Y. Three-stage quantum cryptography protocol under collective-rotation noise. *Entropy* **17**, 2919–2931 (2015).

23. EXFO. FTBx-2850 tunable light source: Specifications. https://www.exfo.com/en/products/lab-manufacturing-testing/tunable-laser-sources/ftbx-2850/specifications. Accessed 18 October 2026.

24. Hollenbeck, D. & Cantrell, C. D. Multiple-vibrational-mode model for fiber-optic raman gain spectrum and response function. *J. Opt. Soc. Am. B* **19**, 2886–2892 (2002).

25. Qi, B., Zhu, W., Qian, L. & Lo, H.-K. Feasibility of quantum key distribution through a dense wavelength division multiplexing network. *New J. Phys.* **12**, 103042 (2010).

26. Ferreira da Silva, T., Xavier, G. B., Temporão, G. P. & von der Weid, J. P. Impact of raman scattered noise from multiple telecom channels on fiber-optic quantum key distribution systems. *J. lightwave technology* **32**, 2332–2339 (2014).

27. Ivan, J. S., Sabapathy, K. K. & Simon, R. Operator-sum representation for bosonic gaussian channels. *Phys. Rev. A* **84**, 042311 (2011).

28. Agnesi, C. *et al.* Simple quantum key distribution with qubit-based synchronization and a self-compensating polarization encoder. *Optica* **7**, 284–290 (2020).

29. Bolaños, M. R. *et al.* Ghz-rate polarization-based qkd system for fiber and satellite applications. *arXiv preprint arXiv:2602.08908* (2026).

30. Xavier, G. *et al.* Experimental polarization encoded quantum key distribution over optical fibres with real-time continuous birefringence compensation. *New J. Phys.* **11**, 045015 (2009).

31. Knill, E. & Laflamme, R. Theory of quantum error-correcting codes. *Phys. Rev. A* **55**, 900 (1997).

5 Conflict of Interest

The authors declare no competing interests.

6 Funding Declaration

This research received no specific funding.

7 Author contributions statement

N.J. proposed the idea and drafted the manuscript. P.P. and A.P. provided intellectual input and research guidance. All authors revised the manuscript.

8 Data Release Statement

The simulation code and generated data are available at the project's GitHub repository.

Supplementary Files

This is a list of supplementary files associated with this preprint. Click to download.

- SupplementaryInformation.tex
- supplementaryrefs.tex
- SupplementaryInformation.pdf